Research article

Journal of RAMAN SPECTROSCOPY

Received: 10 May 2015 Revised: 17 August 2015 Accepted: 28 August 2015 Published online in Wiley Online Library: 8 October 2015

(wileyonlinelibrary.com) DOI 10.1002/jrs.4821

Raman spectroscopic detection for liquid and solid targets using a spatial heterodyne spectrometer

Guangxiao Hu,[a,b,c] Wei Xiong,[a,c]* Hailiang Shi,[a,c] Zhiwei Li,[a,c] Jing Shen[a,b,c] and Xuejing Fang[a,b,c]

Spatial heterodyne Raman spectroscopy (SHRS) is a new type of effective method for the analysis of structure and composition of liquid and solid targets with the characteristics of no moving parts, high spectral resolution, high optical throughput and large field of view. The technique is very suitable for detecting the targets from long distances or under the conditions with ambient light, which is essential for the exploration of planetary surface. In order to have a better understanding of the ability of SHRS for the detection of liquid and solid targets, a breadboard was designed, built and calibrated. Signal to noise was estimated at different integration time or laser power for carbon tetrachloride. Pure materials or materials contained in bottles were both tested. The mixture of organic liquids or inorganic solids were tested. In order to test the detection ability for natural targets, some composition-unknown rocks and pebbles were tested. The results have shown that SHRS can meet the requirements for the detection of weak Raman signal scattered from artificial or natural targets. Standoff detection of sulfur from 5-m or 10-m distance without using any telescope or collimation optics was also tried to test the high optical throughput of SHRS. The potential feasibility of standoff detection has been proved. Copyright © 2015 John Wiley & Sons, Ltd.

Keywords: Raman spectroscopy; spatial heterodyne spectrometer; interference; high spectral resolution; Fourier transform
PACS numbers: 42.62.Fi, 42.30.Kq, 42.25.Hz

Introduction

Raman spectroscopy is an inelastic light scattering technique first discovered by C. V. Raman in 1928.[1,15] Raman spectrum can reflect the structure and composition of many liquid and solid materials in the form of frequency shift, or Raman shift, relative to excitation source, which means that it is invariant for a given target no matter what the frequency of excitation source is. Raman spectroscopy has already been applied to many fields, including chemistry,[2,3] physics,[4,5] biology,[6,7] medicine[8,9] and geology.[10,11]

Because of its capability of detection for liquid and solid targets, especially minerals and organic materials, Raman spectroscopy is very suitable for the application of planetary exploration. Many published results have proved that Raman spectroscopy has the potential feasibility to analyze the composition of minerals (especially carbonates, sulfates, sulfides and silicates) and even has the probability of finding biomarkers (including amino acids, pigments and other organic materials) on the surface of Mars[12–16] or Venus.[17–19]

Currently, most of the Raman detection systems are based on the dispersive grating spectrometers, which have narrow entrance slits to provide the required high resolution. However, the slits limit the optical throughput of the systems, which ultimately affects the detection sensitivity. Conventional step scanning Fourier transform Raman spectrometers can avoid this problem,[20] but because of their moving mirror, they are not compatible with gated detection using pulsed lasers. Many published results[21–23] have proved that gated detection is very essential for the work conditions with strong ambient light or long-life fluorescence.

Spatial heterodyne Raman spectroscopy (SHRS) is a new type of high spectral resolution Raman spectrum analysis technique which combines SHS (the basic theory of SHS can be seen from John M. Harlander's PhD thesis[24]) and Raman spectroscopy, first published by Nathaniel R. Gomer *et al.* in the University of South Carolina[25,26] and T. A. Nathaniel *et al.* in the University of Surrey.[27] The technique has the advantages of high spectral resolution, large field of view and high optical throughput. Spatial heterodyne Raman spectrometer does not have moving parts and can be built with rugged, compact package, making it extremely suitable for space flight and mobile ground instrumentation. Most of the properties are a Raman spectrometer which will work in a harsh environment, particularly, the planetary surface, needed.

Conventional SHS has already been used to learn about the atmospheric environment of our Earth, including monitoring the main greenhouse gases,[28–30] detecting the content of OH,[31,32] measuring the speed of wind,[33,34] etc. Nathaniel R. Gomer and coworkers have indicated that SHS can also be used for the detection of Raman spectra, and they have built a setup of SHRS and achieved

* *Correspondence to: Wei Xiong, Anhui Institute of Optics and Fine Mechanics, Hefei Institutes of Physical Science, Chinese Academy of Sciences, Hefei, Anhui 230031, China.*
E-mail: frank@aiofm.ac.cn

a *Anhui Institute of Optics and Fine Mechanics, Hefei Institutes of Physical Science, Chinese Academy of Sciences, Hefei, Anhui, 230031, China*

b *University of Science and Technology of China, Hefei, Anhui, 230026, China*

c *Key Laboratory of Optical Calibration and Characterization of Chinese Academy of Sciences, Hefei, Anhui, 230031, China*

some results of pure chemicals. But in their research, the SNR of SHRS was not analyzed.

In order to have a better understanding of the properties and detection ability of liquid and solid targets, a breadboard of SHRS has been designed and built in our laboratory. In our breadboard, a Nikon commercial imaging optics with better performance than that used by Nathaniel R. Gomer *et al.* was used to improve the imaging quality of the interferogram, and an Andor CCD with more pixels (1024) along the spatial dimension was used to improve the SNR. The laser power is also smaller than that used by Gomer *et al.* The basic theory of SHRS is provided in the Section Theoretical. Then, a detailed description of the breadboard and calibration results is applied in the Section Experimental. Section Results and discussion gives some results and discussion about the practical tests for organic liquids, inorganics solids and natural targets.

Theoretical

Basic theory

Figure 1 is the schematic of basic SHRS. As we can see, the excitation light from the laser is focused on the target. The Raman, Rayleigh scattered light and fluorescence for some materials are collected and collimated by the collimation lens. Collimated light enters the 50/50 beam splitter and is split into two beams. The separated beams arrive at the diffraction gratings and are diffracted back, re-enter the beam splitter and recombine. The Rayleigh scattered light is filtered by a Raman edge filter or notch filter. The recombined light produces an interference pattern located on the surface of grating G_1 or G_2, which is the Fourier transform of Raman spectrum. According to the basic SHS theory, supposing that the Raman signal from target is $R(\sigma)$, σ_0 is the Littrow wavenumber, θ is the Littrow angle, the interference signal along the direction of the grating diffraction, or the x direction, can be written in Eqn (1)[24] and the spatial frequency is given by Eqn (2):

$$I(x) = \int_0^\infty R(\sigma)(1 + \cos[2\pi(4(\sigma - \sigma_0)x \tan\theta)])d\sigma \quad (1)$$

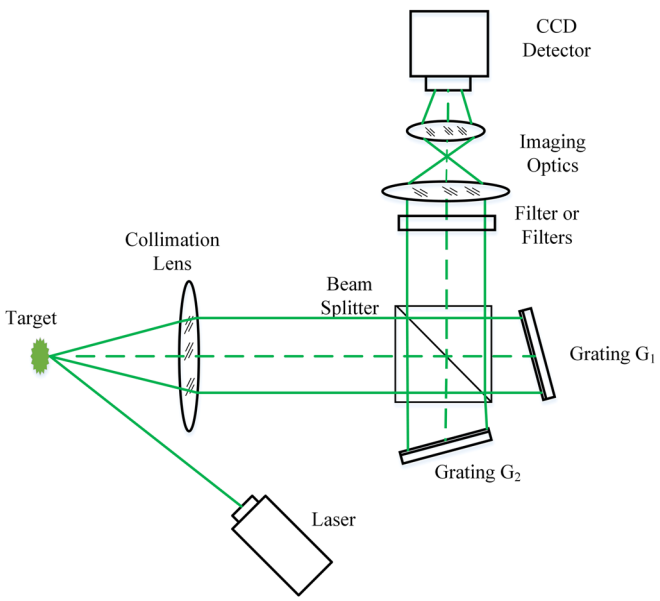

Figure 1. The schematic of basic SHRS.

$$f_x = 4(\sigma - \sigma_0)\tan\theta_L \quad (2)$$

After a one-dimensional Fourier transform, the Raman spectrum can be recovered from the interferogram.

The resolution power R is given by Eqn (3), and the spectral resolution in wavenumber is given by Eqn (4):

$$R = 2GW \quad (3)$$

$$\delta\sigma = \frac{\sigma_0}{R} \quad (4)$$

where G is the grating groove density, and W is the width of illuminated grating.

The spectrum range that can be detected is determined by Eqn (5):

$$\Delta\sigma = \frac{N\delta\sigma}{2} \quad (5)$$

where N is the pixel numbers in the spectral dimension.

From Eqn (2), we can see that the wavenumbers of $(\sigma_0 \pm \sigma)$ have the same spatial frequency with opposite sign. If Littrow wavenumber is set to the laser wavenumber, the recovered Raman Stokes and Anti-Stokes spectra will be overlapped because of the fast Fourier transform operation. In order to avoid this problem, a long-pass (or short-pass) filter should be used to filter out the Anti-Stokes Raman shift (or Stokes Raman shift). In some cases, the Stokes and Anti-Stokes Raman shift are both needed. The Littrow wavenumber can be set as $(\sigma_L - \Delta\sigma/2)$ or $(\sigma_L + \Delta\sigma/2)$ (σ_L is the wavenumber of the laser) to detect the Stokes and Anti-Stokes Raman shift simultaneously. A bandpass filter should be used to filter out the light lower then $(\sigma_L - \Delta\sigma/2)$ and higher than $(\sigma_L + \Delta\sigma/2)$ in wavenumber.

Calibration theory

The actual system performance parameters can be estimated using Eqns (6)–(10).[35]

$$\sigma_0 = \frac{F_2\sigma_1 - F_1\sigma_2}{F_2 - F_1} \quad (6)$$

where σ_0 is the actual Littrow wavenumber, σ_1 and σ_2 are the known wavenumbers from the calibration source, F_1 and F_2 are the measured fringes cycles across the detector width which can be obtained from the fast Fourier transform of the interferogram.

$$\theta = \arcsin\left(\frac{G}{2\sigma_0}\right) \quad (7)$$

where θ is the Littrow angle and G is the grating grooves density.

$$W = \frac{F_1}{4(\sigma_0 - \sigma_1)\tan\theta_L} \quad (8)$$

where W is the width of the interferogram imaged on the detector.

$$\delta\sigma = \frac{\sigma_0}{R} = \frac{\sigma_0}{2GW} \quad (9)$$

where $\delta\sigma$ is the actual spectral interval, R is the actual resolution power.

$$\sigma(F) = \sigma_0\left(1 - \frac{F}{2GW}\right) \quad (10)$$

where F is a measured fringes cycles across the detector width, and $\sigma(F)$ is the wavenumber corresponding to the given

Journal of RAMAN SPECTROSCOPY

F. Equation (10) gives the wavenumber as a liner function of measured fringes cycles.

Experimental

Breadboard

The key parameters of the components used in the experimental breadboard (Fig. 2) are listed in Table 1. All components are commercial off-the-shelf products. The active area of the two gratings (Edmund Optics #64-402) was 14 mm × 14 mm. The effective pixel numbers of the charge coupled device (CCD, Andor, iKon-M) were 800 × 800. The laser power operated from 0 to 318 mW (Laser: Changchun Laser Optoelectronic Technology Co, Ltd. MW-ZGL-532/300mW).

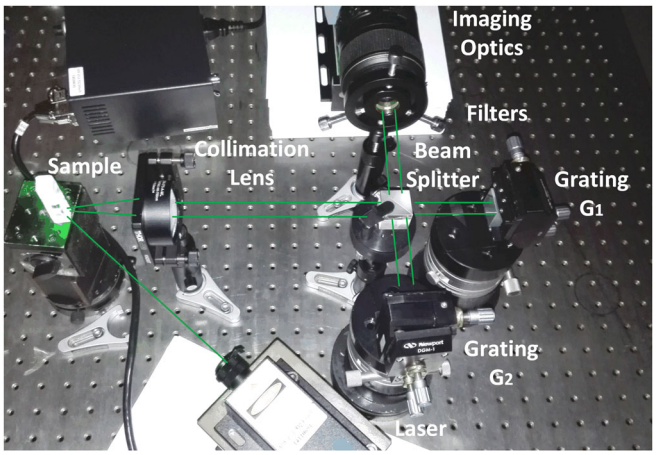

Figure 2. The layout of the experimental breadboard.

Table 1. The key parameters of the components used in the experiment breadboard

Components	Main parameters	Performance index
Laser	Wavelength	532 nm, CW
	Spectral linewidth (nm)	<0.1
	Beam diameter (1/e2, mm)	~1
	Beam divergence (full angle, mrad)	<1.5
Gratings	Groove density	150 groove/mm
	Ruled area	25×25 mm^2
Beam splitter	Size	$25 \times 25 \times 25$ mm^3
CCD	Pixel numbers	1024×1024
	Pixel size	13×13 μm^2
Collimation lens	Diameter	50 mm
	Focal length	75 mm
Imaging lens	Diameter	62 mm
	Focal length	105 mm
532-nm	Edge wavelength	533.3 nm
long-pass	Transition width	90 cm^{-1}
edge filter	Blocking band	$OD_{abs} > 6$@532 nm
532-nm	Notch bandwidth	17 nm
notch filter	Blocking band	$OD_{abs} > 6$@532 nm
575-nm	Edge wavelength	575 nm
short-pass filter	Optical density	≥4

In the experiment, liquid samples in a quartz cuvette or solid samples put on a paper plate were placed on the focus plane of the collimation lens (Thorlabs, AC-508-075-A). The angle between the laser and optical axis was about 135°. A 532-nm long-pass edge filter (Semrock LP03-532RE-25) was used to filter out the Rayleigh light, laser light, Anti-Stokes Raman shift bands and ambient light lower than 532 nm in wavelength. A 575-nm short-pass edge filter (Edmund Optics #84-709) was used to filter out the ambient light or fluorescence higher than 575 nm in wavelength. In some results, another 532-nm notch filter (Semrock NF-01-532U-25) was used to filter out the strong laser background when the Raman signal of the target was weak. The cooled temperature of the CCD was set to −50 °C, and the room temperature was about 25 °C. All lights were turned off to decrease the ambient light.

According to Eqns (3)–(5), if the Littrow wavelength is set to 532 nm, the theoretical spectral interval is 4.5 cm^{-1}, the maximum Raman shift that can be detected is 1800 cm^{-1} Stokes Raman shift (Anti-Stokes Raman shift is filtered). Considering the transition width of the 532-nm long-pass edge filter and the 575 nm short-pass edge filter, the actual Raman shift can be detected is 63–1308 cm^{-1}. Additionally, we can get a higher resolution by replacing the gratings with higher groove density.

Comparison of SNR of SHRS with conventional dispersive spectrometer

The limiting field of view of SHRS, or Ω_{max}, is the same as that of the conventional Fourier transform Raman spectrometers and is given by Eqn (11):

$$\Omega_{max} = 2\pi/R \tag{11}$$

For a dispersive spectrometer, the limiting field half-angle, or β_{DS}, can be expressed as Eqn (12):[36]

$$\beta_{DS} = \arctan\left(\frac{W_s}{2f'}\right) \tag{12}$$

where W_s is the width of the dispersive spectrometer's slit and f' is the focus length of the dispersive spectrometer's collimating lens system.

If the slit has a height of h, the half-angle of the resulting ray bundle in the direction normal to the plane of dispersion after collimation, or β_H, can be written as Eqn (13):[36]

$$\beta_H = \arctan\left(\frac{h}{2f'}\right) \tag{13}$$

To get an effective angle with which to calculate the approximate acceptance field of view, take the geometric mean of the vertical and horizontal half-angular divergences:[36]

$$\beta_{eff} = \sqrt{\beta_H \beta_{DS}} \tag{14}$$

The field of view at some field half-angle β can be expressed as Eqn (15):

$$\begin{aligned} \Omega &= 2\pi(1 - \cos\beta) \\ &\approx \pi\beta^2 \ (\text{for small } \beta) \end{aligned} \tag{15}$$

For a conventional Czerny Turner dispersive spectrometer, the required width of the slit is given by Eqn (16):[37]

$$W_s = \frac{\delta\lambda n W_P}{R_{SF}\Delta\lambda} \tag{16}$$

where $\delta\lambda$ is the target spectral resolution in wavelength, $\Delta\lambda$ is the bandpass of the spectrometer, n is the number of detector pixels, W_P is the pixel width and R_{SF} is the resolution factor (assumed to be 1).

Therefore, to achieve the same spectral resolution and spectral bandpass, assuming the same detector is used ($n = 1024$), the instrument must have a slit of less of 33 μm.

Assuming W_s equals to 33 μm, h equals to 5 mm and f' equals to 75 mm (equals to that of our SHRS), then we can get:

$$\beta_{eff} = 0.16^{\circ}$$

To our SHRS, the theoretical R equals to 4177, so:

$$\beta_{SHRS} = 1.25^{\circ}$$

The SNR of SHS can be predicted as (shot noise limited) Eqn (17):[24]

$$SNR_{SHRS} = \sqrt{\frac{\varepsilon A\Omega}{2N} I\delta\sigma T} \tag{17}$$

where ε is the optical efficiency, A is the effective area of the system, N is the number of samples ($N = 400$ in our SHRS), I is the intensity of the continuum in photons per second per unit area per steradian per unit wavenumber (I is in proportion to the laser power for Raman detection), $\delta\sigma$ is the spectral resolution and T is the total integration time.

The SNR of conventional dispersive spectrometer can be predicted as (shot noise limited):

$$SNR_{DS} = \sqrt{\frac{\varepsilon A\Omega}{N} I\delta\sigma T} \tag{18}$$

Therefore, from Eqns (11)–(18), assuming the same ε, A, N, I, $\delta\sigma$ and T are achieved, we can know that:

$$\frac{SNR_{SHRS}}{SNR_{DS}} = \sqrt{\frac{1}{2}}\frac{\theta_{SHRS}}{\theta_{eff}} = 5.5$$

We have to mention that our breadboard is a non-field-widened system, if a field-widened system is used, β can be re-written as Eqn (19):

$$\beta = \sqrt{2/R}\cot(\alpha/2) \tag{19}$$

where α is the apex angle of the field-widening prisms. The value of β of a field-widened SHRS often can be about 10 times of that of a non-field-widened system; thus, a larger SNR can be achieved. A detailed theory of field-widening can be seen from References 24 and 31.

Calibration

A low pressure mercury lamp was used to be the calibration lamp because its three mercury emission lines of 546.075 nm, 576.961 nm and 579.067 nm are in the bandpass (no filter was added). The raw interferogram (a), a cross section of the raw interferogram (b) and the recovered spectrum (c) are shown in Fig. 3.

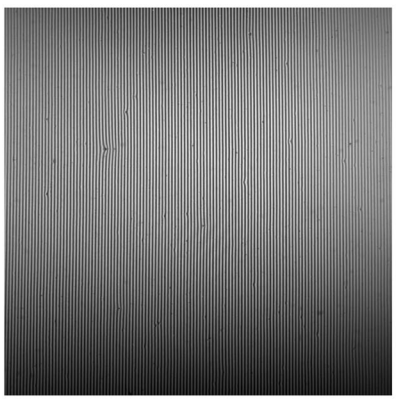

(a)

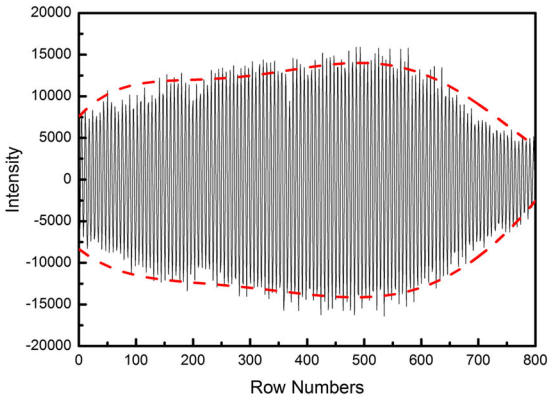

(b)

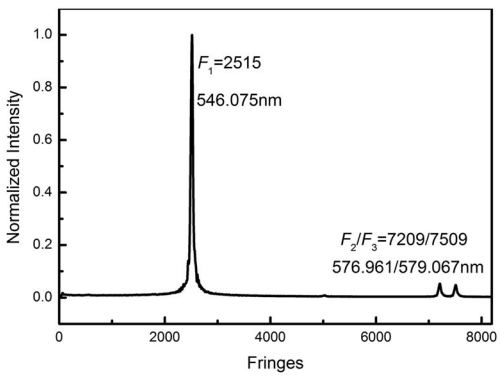

(c)

Figure 3. (a) The raw interferogram of low pressure mercury lamp. (b) A cross section of the raw interferogram. (c) The recovered spectrum of mercury lines. A total of 800 lines recovered spectra can be obtained through the operations of flatfielding, zero filling (16 384 points), phase correction and fast Fourier transform for the raw interferogram. After an 800 lines average operation to the 800 lines recovered spectra, the spectrum shown in (c) can be achieved.

Journal of RAMAN SPECTROSCOPY

According to Eqns (6)–(9), the Littrow wavenumber can be estimated to 18 840 cm^{-1} (530.79 nm), the spectral interval can be estimated to 4.3 cm^{-1} and the spectrum range can be estimated to 1720 cm^{-1}, which are all near to the theoretical values. The full width at half maximum (FWHM) of 546.075 nm is about 10 cm^{-1}, which can be seen as the actual spectral resolution and is a little more than the theoretical spectral interval. The main reasons causing the broadening of the spectral lines include the finite sampling of the interferogram and the nonuniform illumination. The finite sampling caused by the finite pixels of the detector can broaden the FWHM of a spectral line to about 1.21 times than ideal FWHM. The nonuniform illumination, which can be seen from the interferogram and cross section obviously, produces an envelope function multiplied to the interferogram; this contributed a lot to the broadening of the spectral lines.

Results and discussion

SNR analysis for CCl_4

Figure 4 shows two raw interferograms at two different laser power of 196 mW (a) and 6 mW (b) with an integration time of 30 s, two interferogram cross sections (with flatfielding) (c) and two Raman spectra (d) generated by taking one-dimensional fast Fourier transform to the interferograms (with flatfielding, 16384-points zero filling and phase correction) for carbon tetrachloride (CCl_4). The *x* label of the Raman spectra is determined by Eqn (10). The arrows above each spectrum refer to the appropriate intensity axis for that spectrum.

From the Raman spectrum at 196 mW, we can clearly recognize the weak Raman shifts at 762 cm^{-1} and 790 cm^{-1}. The 218 cm^{-1}, 314 cm^{-1} and 459 cm^{-1} Stokes Raman shifts can be clearly recognized at both laser power. At 6 mW, although the interferogram is badly influenced by the CCD noise and laser speckle and ambient light passed through the filters, and nearly no interference information can be seen from the cross-sections, after 800 lines average operation to the recovered spectra of 800 lines cross sections, the signal is high enough to identify the strong Raman peaks. It proves that SHRS has an excellent sensitivity. But we can also see that when the Raman scattered signal is weak, the recovered spectrum has some noise peaks which will disturb the recognition of Raman peaks.

A phenomenon we have to mention is that the intensity of 459 cm^{-1} is smaller than that published by some other researchers, and it makes the intensities of 218 cm^{-1}, 314 cm^{-1} and 762/790 cm^{-1} seem larger than the expected values. We think the main reason causing the phenomenon is the polarization effect from the 135° observation direction.

The set of Raman active vibrational modes of CCl_4 is given by:[38]

$$\Gamma_{vib} = A_1 + E + T_1 + T_2 \tag{20}$$

The meaning of Mulliken Symbols A_1, E, T_1 and T_2 can be seen from Reference 39.

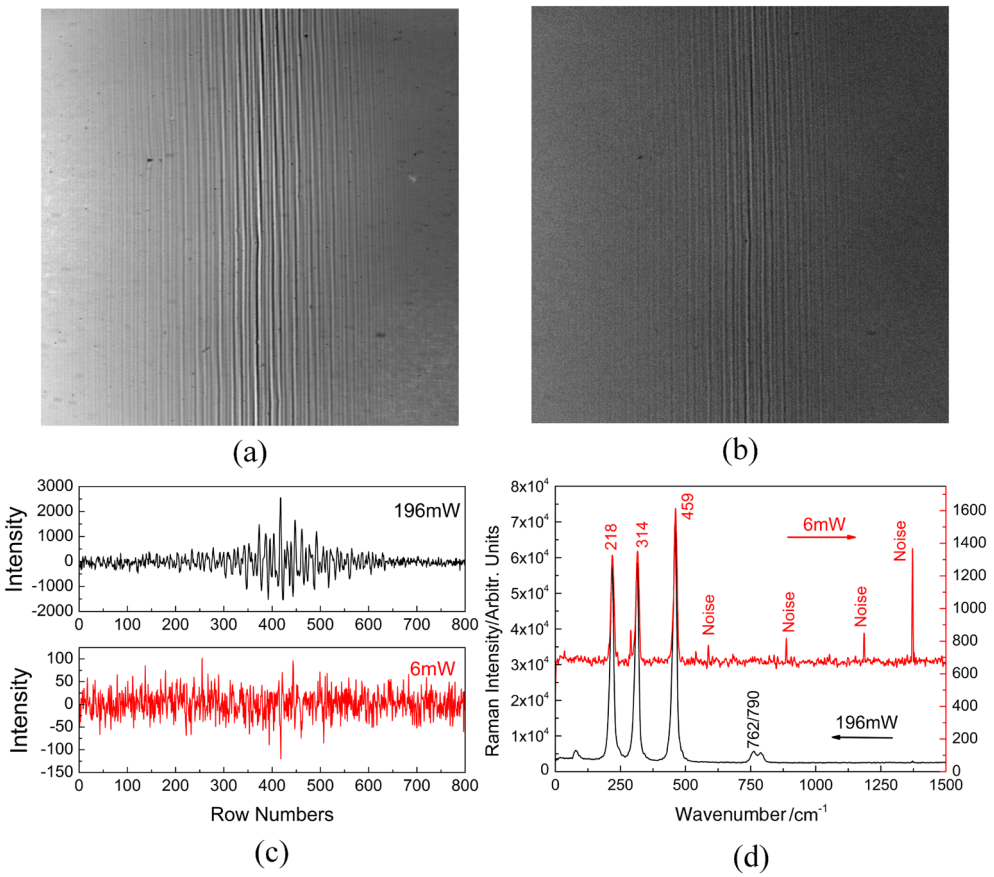

Figure 4. (a) The raw interferogram for CCl_4 at the laser power of 196 mW. (b) The raw interferogram for CCl_4 at the laser power of 6 mW. (c) Two interferogram cross sections. (d) Two recovered Raman spectra of CCl_4.

The four (1 A_1, 1 E, 1 T_1 and 1 T_2) normal modes of vibration are assigned to the bands of 459 cm^{-1}, 218 cm^{-1}, 790 cm^{-1} and 314 cm^{-1} in the CCl_4 spectrum, respectively. A fifth band at 762 cm^{-1} is assigned the combination mode $T_2 + A_1$.

Because the 459 cm^{-1} belongs to the totally symmetric A_1 species and contains the polarization information of the incident laser light, the observed intensity is dependent to the observation direction. If an observation direction of 90° is used, the observed relative Raman intensity of 459 cm^{-1} will decrease dramatically (not shown in this article).

The noise is calculated by measuring the standard deviation in the spectrum beyond 1000 cm^{-1} in the recovered spectrum for CCl_4. This value is then divided by the amplitude of 459 cm^{-1} Raman peak, which resulting in a measured SNR. Figure 5 gives the measured SNR at different integration time with the same laser power of 196 mW (a) or at different laser power with the same integration time of 30 s (b). From Fig. 5(a), we can see that when the integration time is shorter than 20 s, the SNR grows rapidly with the increase of integration time. However, when the integration time is longer than 20 s, the increase of SNR is not obvious. From Fig. 5(b), we can see that when the laser power is smaller than 250 mW, the SNR appears to increase linearly with laser power; when the laser power is larger than 250 mW, the SNR nearly stops increasing. The SNR plot in Fig. 5(a) is similar to a square-root function, which coincides with Eqn (17). However, the SNR plot in Fig. 5(b) does not seem so. The thorough reasons for this are not clear, but one of the reasons may be that the noise at low laser powers is dominated by a constant factor, such as detector dark current or ambient light, that is independent of the laser power. In this case, the shot noise is not a major limitation of the system. When detecting different kinds of targets, different laser powers and integration times are needed.

Artificial target detection

Figure 6(a) shows Raman spectra of pure powder sulfur contained in a plastic bottle or in the plastic bottle packaged by two pieces of plastic bubble wrap or four pieces of plastic bubble wrap. The thickness of the plastics bottle is about 1 mm and the main ingredient is white high density polyethylene. The first two spectra are achieved at the laser power of 110 mW and the integration time of 1 s, and the third spectrum is achieved at the laser power of 196 mW and the integration time of 5 s. There is nearly no spectral resolution difference in the three spectra. However, obviously, the SNR is lower, which is caused by the laser reflection light or fluorescence from the plastic bubble wrap. If more thick bottles or more pieces of plastic bubble wrap are used, larger laser powers or longer integration times are required. Figure 6(b) shows two Raman spectra of pure potassium sulfate (K_2SO_4) and K_2SO_4 contained in a transparent glass bottle. The thickness of the bottle is about 3 mm. Both of the spectra are achieved at a laser power of 196 mW and an integration time of 30 s. An obvious broadband fluorescence background added to the Raman spectrum is detected for the K_2SO_4 contained in the glass bottle, but the Raman peaks are still strong enough to be recognized. From Fig. 6(a) and 6(b), we can see that SHRS has the ability to detect targets contained in plastic or glass containers, which is very important to

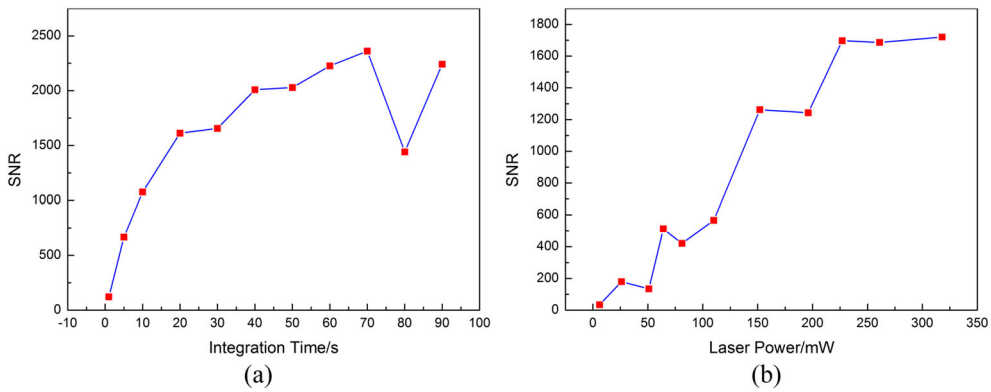

Figure 5. (a) The measured SNR at different integration time with the same laser power of 196 mW. (b) The measured SNR at different laser powers with the same integration time of 30 s.

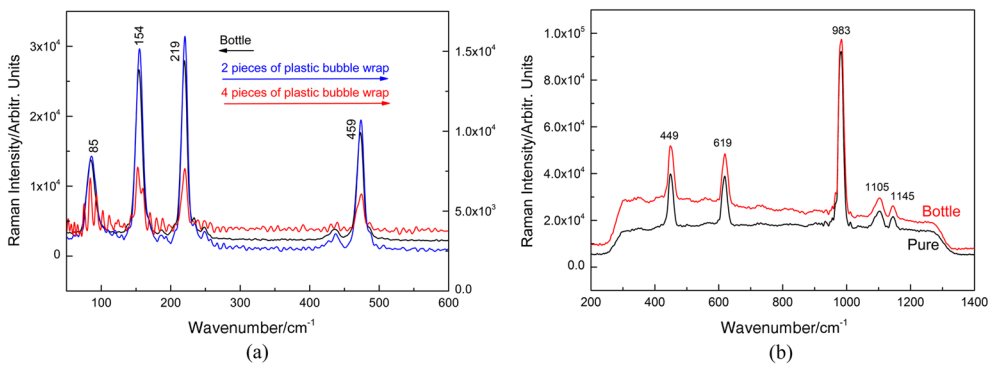

Figure 6. (a) Raman spectra of powder sulfur in a plastic bottle or in a plastic bottle packaged by two pieces of plastic bubble wrap or four pieces of plastic bubble wrap. (b) Raman spectra of pure potassium sulfate and potassium sulfate contained in a glass bottle.

Journal of RAMAN SPECTROSCOPY

the practical applications, such as the detection of dangerous explosives or chemicals which contained in plastic or glass containers that cannot be opened.

Figure 7(a) shows Raman spectra of four organic liquids, CCl_4, cyclohexane, acetone, ethyl alcohol and a mixture of the four organic liquids. A 532-nm notch filter was added to remove the strong Rayleigh scattered light relative to the weak Raman signal. The black line represents the continuous spectrum response of an integrating sphere with continuous white light; the wavy pattern in the spectrum is caused by the shape of the filters' transmission curve and can be seen more clearly in Fig. 7(c). The red curve represents the ideal transmission curve of the filters. The wavy shake in the spectrum of white light quite coincides with that of the transmission curve. When the targets with strong fluorescence background are detected, the wavy shake can also appear in their spectra (such as those being shown in Figs. 8 and 9). This interference pattern can be avoided by using filters with more flat transmission curves and careful radiometric calibration. In the spectra of CCl_4, cyclohexane and acetone, the main Raman peaks are well detected. In the spectrum of ethyl alcohol, a strong broadband fluorescence background influences the recognition of Raman peaks, but strong Raman peaks can be clearly seen. Because of the limitation of spectral resolution, the strong fluorescence of ethyl alcohol and the intensity difference of different organic materials, only the 314 cm^{-1} and 459 cm^{-1} of CCl_4, 884 cm^{-1} of ethyl alcohol and 1029 cm^{-1} and 1267 cm^{-1} of cyclohexane can be well distinguished in the spectrum of the mixture. The spectral resolution of about 10 cm^{-1} cannot distinguish 786 cm^{-1} of acetone, 790 cm^{-1} of CCl_4 and 803 cm^{-1} of cyclohexane. The strong fluorescence of ethyl alcohol has flooded the weak Raman peaks of acetone. The strong Raman signal of CCl_4 and cyclohexane has nearly completely masked the Raman signal of ethyl alcohol and acetone.

Figure 7(b) shows Raman spectra of four inorganic solids, K_2SO_4, gypsum ($CaSO_4{\cdot}2H_2O$), calcium carbonate ($CaCO_3$), ammonium nitrate (NH_4NO_3) and a mixture of the four solids. In the spectra of pure solids, the main Raman peaks are well distinguished. Compared to organic liquids, the inorganic solids bear a less influence from strong fluorescence. The main Raman peaks of every pure solids are well recognized in the spectrum of the mixture.

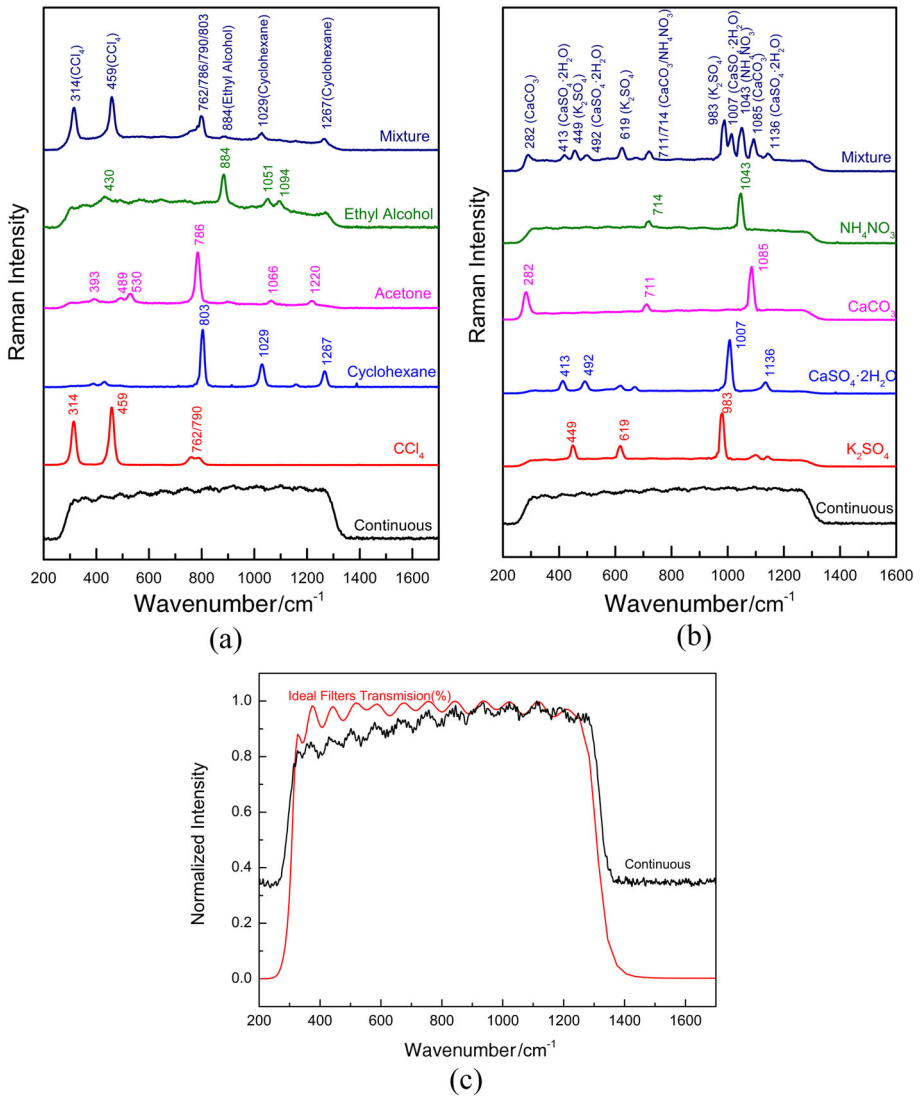

Figure 7. (a) Raman spectra of organic liquids. (b) Raman spectra of inorganic solids. Laser power: 196 mW. Integration time: 30 s. (c) the filters' transmission curve and the continuous spectrum response of an integrating sphere with continuous white light.

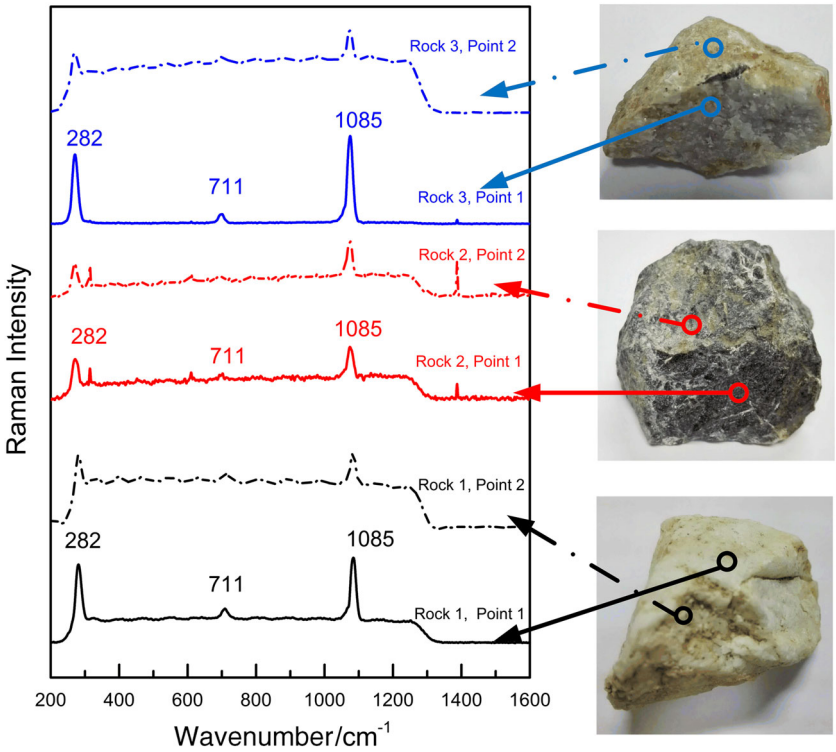

Figure 8. Raman spectra of three natural rocks. Rock 1: at the laser power of 196 mW and the integration time of 10 s. Rock 2: at the laser power of 318 mW and the integration time of 30 s. Rock 3: at the laser power of 318 mW and the integration time of 10 s.

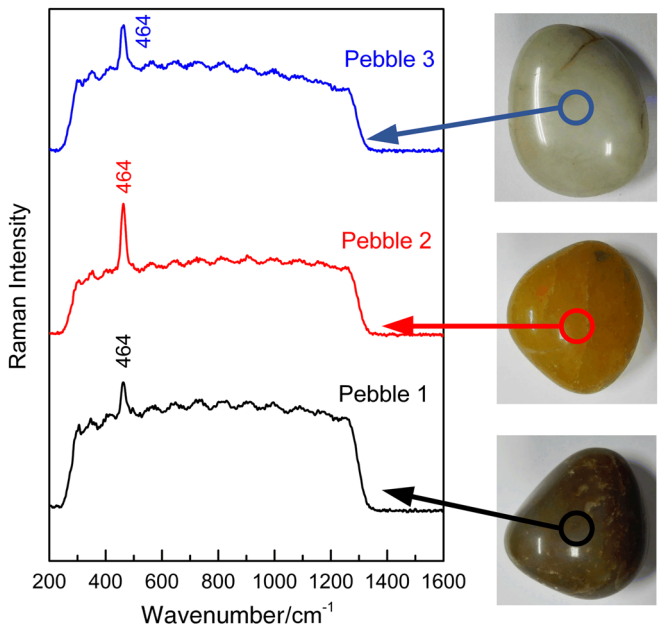

Figure 9. Raman spectra of three natural pebbles.

Natural target detection

In order to test the detection ability of natural targets, several composition-unknown rocks and pebbles were tested. Figure 8 shows Raman spectra of three rocks, every rock takes two sampling points. Although the rocks look very different, we can judge that they all contain carbonate from the Raman spectra. The sampling point 2 of every rock is badly polluted by soil or some composition-unknown materials, which produces a strong fluorescence background. The surface of sampling point 1 of every rocks is removed, so the Raman spectra bear a less influence of fluorescence. The fluorescence caused by the pollutant covered in the surface of natural targets will be a great problem that needs to be solved in the future research.

Figure 9 shows Raman spectra of three natural pebbles. The laser power was 318 mW, and the integration time was 10 s in all of the three tests. The 464 cm^{-1} of quartz is detected in all of the three pebbles. The strong background in the peddle spectra may come from the fluorescence which is caused by the different kinds impurities contained on the surfaces of the pebbles.

Anti-Stokes band detection

In order to test the anti-Stokes bands, a 532-nm notch filter was used to replace the edge filter, and the Littrow wavenumber was moved to one side away 532 nm about −880 cm^{-1}. Figure 10 shows Raman spectra of sulfur (a) and CCl_4 (b). Because of the restrict of notch filter, the Stokes Raman shift below 280 cm^{-1} and the anti-Stokes Raman shift below 325 cm^{-1} are filtered, so a wide bandpass (about one third of the whole bandpass) is wasted. However, if a notch filter with better performance index applied, the whole bandpass can be increased and the notch bandwidth will have a little influence. Because of the strong back scattered light of Rayleigh of powder sulfur, a strong laser line is detected. When other solids with weak Raman scattering are detected, the strong Rayleigh will be a serious problem. To solve this, another one or two notch filters should be added. The back scattering of Rayleigh of liquids is not as strong as solids, so the spectrum of CCl_4 is not influenced. The low pressure mercury lamp cannot be used as calibration lamp because its 576.961-nm and 579.067-nm lines are out of the bandpass, so the Raman peaks of sulfur are used as

Journal of RAMAN SPECTROSCOPY

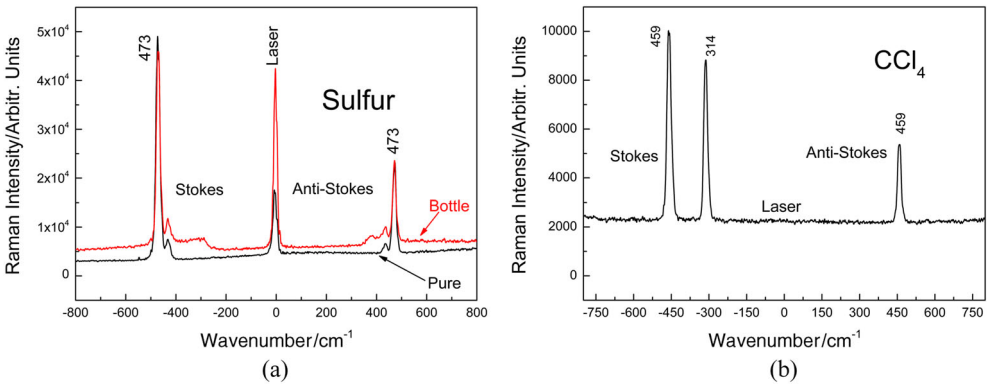

Figure 10. (a) Raman spectra of sulfur. (b) Raman spectrum of carbon tetrachloride.

calibration lines to determine the *x* label. Another phenomenon that has to be considered is that the intensity ratios of anti-Stokes *versus* Stokes Raman peaks are higher than the expected ratios based on Boltzmann distribution. In theory, the ratio of 473 cm^{-1} equals to 0.10 and the ratio of 459 cm^{-1} equals to 0.11 at the temperature of 25 °C. However, the ratios are 0.47 (pure sulfur), 0.50 (sulfur in container) and 0.53 (CCl_4). The difference may be caused by the decreased instrumental response at the Stokes band. The Littrow wavenumber is set at the anti-Stokes band, so the interferograms of the Raman peaks in the anti-Stoke band have smaller spatial frequencies than those in the Stokes band. Limited by the modulation transfer function of imaging optics and poor adjustments, the instrumental response will be decreased for the Stokes band because of the larger spatial frequencies, so the detected intensity of the Stokes band is smaller than the ideal values, which results in the increase of the intensity ratios.

Standoff detection

Figure 11 shows the detected interferograms of sulfur contained in a plastics bottle from a distance of about 5 m (a) or 10 m (b) and the recovered spectra (c). Because the focus length of collimation lens in Fig. 2 was too short relative to a 5-m or 10-m distance, the collimation lens was removed and no telescope or collimation optics was used in the test, so only a small solid angle is collected. Although the whole gratings were still illuminated, only low intensity light could arrive at the edge of the gratings, and only the central area of the interferogram can be clearly seen. All lights were turned off to decrease the ambient light. The diameter of the laser point was 7 mm at the distance of 5 m and the laser power was 196 mW with an integration time of 60 s, so the laser power density at the sample was about 509 mW/cm^2, which was about 0.0204 time of the laser power density *in situ* (196 mW with an integration time of 1 s). The diameter of the laser point was 16 mm at the distance of 10 m and the laser power was 318 mW with an integration time of 60 s, so the laser power density at the sample was about 404 mW/cm^2, which was about 0.016 time of the laser power density *in situ*. Even so, the Raman signal could be detected with a relatively long integration time and the strong Raman peaks could be recognized from the spectra. We have to mention that the laser power density is still very high to the detection of some light-degradation materials or explosives, but if a telescope is used, the laser power density could be decreased dramatically. The standoff SHRS using a telescope is under building; some more detailed experimental results may be

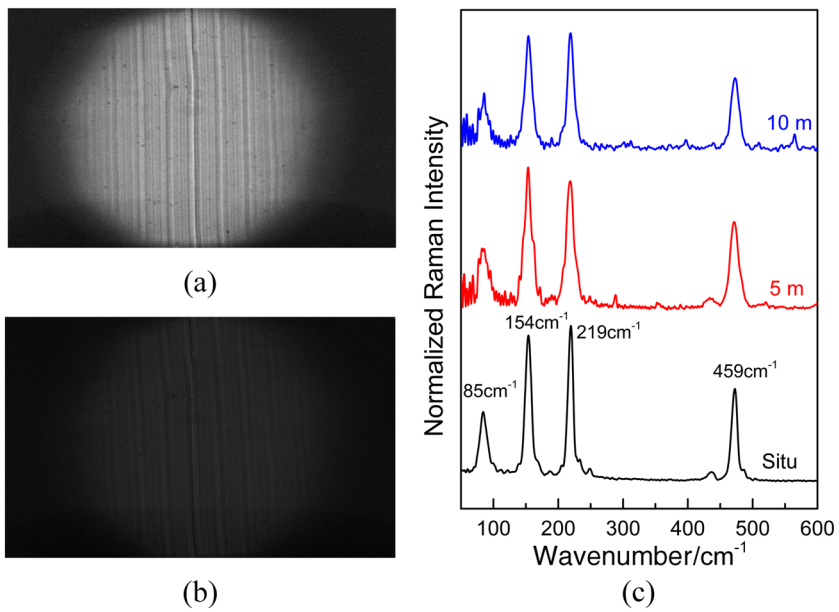

Figure 11. (a) The detected interferogram of sulfur contained in a plastics bottle from a distance of about 5 m. (b) The detected interferogram of sulfur from a distance of about 10 m. (c) The recovered spectra from the left interferograms and a spectrum detected *in situ*.

applied in our future research. The result shown at here is far away from a practical standoff SHRS, but it can still prove that SHRS has a good optical throughput and sensitivity, partially.

Impact of SHRS on health and safety

From the results shown above, we can find that most of the spectra are achieved at a laser power higher than 100 mW. It is dangerous for the health and safety of operators and the public if no protection measure is used, especially in the situ detection. *In situ*, the laser point is only about 1 mm, so the laser power density is more than 10 W/cm^{-1}. Such a big laser power density will cause a great harm if the laser light enters our eyes directly. In the standoff detection, the laser power density is lower, but still cannot satisfy the requirement of no harm to humans.

The most likely reason of requiring such a big laser power of our SHRS is the poor sensitivity of CCD for Raman spectroscopic detection. We plan to use an Intensified-CCD to replace the CCD used in the article if we can get enough financial support in the future research.

Another way that can decrease the laser power is using a field-widened SHRS. As analyzed in the Section Experimental, we have known that if a field-widened system is used, the value of field half-angle β of a field-widened SHRS often can be about 10 times of that of a non-field-widened system, so a lower laser power is needed.

Conclusion

A breadboard for Raman spectroscopic detection based on spatial heterodyne spectroscopy has been designed and built to prove the detection ability of SHS in liquid and solid targets. Although the breadboard is not ideal because of the poor adjustment and experiment conditions, the results have shown the excellent ability of SHRS. From the experiment result, we can see that if the laser power and integration time are set appropriately, a SNR more than 1000 can be achieved. Some results have also proved that SHRS has the ability to detect the targets contained in plastic or glass bottles. In situations where the containers cannot be opened, this is very important. In order to test the detection ability to mixed targets, the mixture of organic liquids or inorganic solids was tested. In order to test the detection ability of natural targets, some composition-unknown rocks and pebbles were tested. The results prove that SHRS has a good ability to detect artificial and natural targets. The ability of SHRS to detect anti-Stokes also has been proved, but because of the wide notch bandwidth of the filter, a wide bandpass (about one third of the whole bandpass) was wasted. The standoff detection was also tried, and the Raman signal was detected without the help of any telescope or collimation optics. The standoff SHRS for planetary exploration will be the focus of a future study.

Acknowledgements

The authors of this study would like to thank Key Laboratory of Optical Calibration and Characterization of the Chinese Academy of Sciences for funding this research. Authors extend thanks to Haiyan Luo, Shuang Li, Jin Hong and Hongchun Yang for their valuable suggestion in our research sincerely.

References

[1] C. V. Raman, *Nature* **1928**, *121*, 69.
[2] E. C. Cull, M. E. Gehm, B. D. Guenther, D. J. Brady, *Proc. SPIE* **2005**, *5994* 59940H-1.
[3] M. Wu, M. Ray, K. H. Fung, M. W. Ruckman, D. Harder, A. J. Sedlack III, *Appl. Spectrosc.* **2000**, *54*, 800.
[4] K. J. Baustian, Using Raman spectroscopy and optical microscopy to investigate cirrus cloud formation. PhD Thesis, University of Colorado, Colorado, **2011**.
[5] T. Somekawa, T. Takeuchi, C. Yamanaka, M. Fujita, *Proc. SPIE* **2014**, *9240*, 92400J-1.
[6] K. Moor, H. K. Hashimoto, M. Sawa, B. B. Andriana, K. Ohtani, T. Yagura, H. Sato, *Proc. SPIE* **2013**, *8587*, 85871X-1.
[7] I. H. Boyacı, H. T. Temiz, R. S. Uysal, *Food Chem.* **2013**, *148*, 37.
[8] C. A. France, D. B. Thomas, C. R. Doney, O. Madden, *J. Archaeol. Sci.* **2014**, *42*, 346.
[9] H. Wang, M. A. Boraey, L. Williams, D. Lechuga-Ballesteros R. Vehring, *Int. J. Pharmaceut.* **2014**, *469*, 197.
[10] J. D. Stopar, P. G. Lucey, S. K. Sharma, A. K. Misra, G. J. Taylor, H. W. Hubble, *Spectrochim. Acta A.* **2005**, *61*, 2323.
[11] A. K. Misra, S. K. Sharma, C. H. Chio, P. G. Lucey, B. Lienert, *Spectrochim. Acta A.* **2005**, *61*, 2281.
[12] A. Wang, L. A. Haskin, A. L. Lane, T. J. Wdowiak, S. W. Squyres, L. E. Holland, K. S. Manatt, N. Raouf, C. D. Smith, *J. Geophys. Res.* **2003**, *108*, E1.
[13] J. Wei, A. Wang, J. L. Lambert, D. Wettergreen, N. A. Cabrol, K. Warren-Rhode, the LITA team, 45th Lunar and Planetary Science Conference, Texas, USA, March 17–21, **2014**.
[14] J. Wei, A. Wang, J. L. Lambert, D. Wettergreen, N. A. Cabrol, K. Warren-Rhode, the LITA team, 11th International GeoRaman Conference, Missouri, USA, June 15–19, **2014**.
[15] I. B. Hutchinson, M. Edwards, R. Ingley, L. Harris, M. McHugh, C. Malherbe, J. Jehlicka, C. Marshall, J. Parnell, 11th International GeoRaman Conference, Missouri, USA, June 15–19, **2014**.
[16] F. Rull, the RLS team, Eighth International Conference on Mars, California, USA, July 14–18, **2014**.
[17] J. Lambert, J. Morookian, T. Roberts, J. Polk, S. Smrekar, S. M. Cledd, R. C. Wiens, M. D. Dyar, A. Treiman, 41th Lunar and Planetary Science Conference, Texas, USA, March 1–5, **2010**.
[18] S. K. Sharma, A. K. Misra, P. G. Luccy, R. C. Wiens, S. M. Clegg, *Spectrochim. Acta A.* **2007**, *68*, 1036.
[19] S. K. Sharma, A. K. Misra, S. M. Clegg, J. E. Barefield, R. C. Wiens, T. E. Acosta, D. E. Bates, *Spectrochim. Acta A.* **2011**, *80*, 75.
[20] S. Dzsaber, M. Negyedi, B. Bernáth, B. Gyüre, T. Fehér, C. Kramberger, T. Pichler, F. Simon, *J. Raman Spectrosc.* **2015**, *46*, 327.
[21] S. K. Sharma, P. G. Lucey, M. Ghosh, H. W. Hubble, K. A. Horth, *Spectrochim. Acta A.* **2003**, *59*, 2391.
[22] A. K. Misra, S. K. Sharma, T. E. Acosta, J. N. Porter, D. E. Bates, *Appl. Spectrosc.* **2012**, *66*, 1279.
[23] J. H. Chung, S. G. Cho, *Proc. SPIE* **2013**, *8709*, 87090s-1
[24] J. M. Harlander, Spatial heterodyne spectroscopy: interferometric performance at any wavelength without scanning. PhD Thesis, University of Wisconsin-Madison, Madison, **1991**.
[25] N. R. Gomer, C. M. Gordon, P. Lucey, S. K. Sharma, J. C. Cater, S. M. Angel, *Appl. Spectrosc.* **2011**, *65*, 849.
[26] N. R. Gomer, The development of a spatial heterodyne spectrometer for Raman spectroscopy. PhD Thesis, University of South Carolina, USA, **2012**.
[27] T. A. Nathaniel, C. I. Underwood, 42th Lunar and Planetary Science Conference, Texas, USA, March 7–11, **2011**.
[28] J. Wu, X. Wang, Y. Fang, W. Xiong, H. Shi, Y. Qiao, *Acta. Optica. Sinica.* **2011**, *31*, 0101001–1.
[29] W. Xiong, H. Shi, Y. Wang, H. Luo, Y. Fang, Y. Qiao, *Acta. Optica. Sinica.* **2010**, *30*, 1511.
[30] Y. Lin, Instrument development for spatial heterodyne observations of water. PhD Thesis, York University, Canada, **2010**.
[31] J. M. Harlander, F. L. Roesler, J. G. Cardon, C. R. Englert, R. R. Conway, *Appl. Optics* **2002**, *41*, 1343.
[32] C. R. Englert, M. H. Stevens, D. E. Siskind, J. M. Harlander, F. L. Roesler, *J. Geophys. Res.* **2010**, *115*, D20306.
[33] C. R. Englert, J. M. Harlander, D. D. Babcock, M. H. Stevens, D. E. Siskind, *Proc. SPIE.* **2006**, *6303*, 63030T-1.
[34] C. R. Englert, D. D. Babcock, J. M. Harlander, *Appl. Optics* **2007**, *46*, 7297.
[35] C. R. Englert, J. C. Owrutsky, J. M. Harlander, *Nav. Res. Lab.*, **2005**, NRL/MR/7640–05-8926, 1.
[36] C. N. Pannell, B. G. Zhang, M. K. Reed, *Proc. SPIE.* **2015**, *9369*, 936903–1.
[37] M. Foster, J. Storey, P. Stockwell, D. Widdup, *Opt. Express*, **2015**, *23*, 3027.
[38] David Tuschel, *Spectroscopy* **2014**, *29*(3), 15.
[39] David Tuschel, *Spectroscopy* **2014**, *29*(2), 14.